nature nanotechnology

ARTICLES

https://doi.org/10.1038/s41565-021-00919-y

Flexo-photovoltaic effect in MoS_2

Jie Jiang[1]✉, Zhizhong Chen[1], Yang Hu[1], Yu Xiang[2], Lifu Zhang[1], Yiping Wang[1], Gwo-Ching Wang[2] and Jian Shi[1]✉

The theoretical Shockley–Queisser limit of photon–electricity conversion in a conventional p–n junction could be potentially overcome by the bulk photovoltaic effect that uniquely occurs in non-centrosymmetric materials. Using strain-gradient engineering, the flexo-photovoltaic effect, that is, the strain-gradient-induced bulk photovoltaic effect, can be activated in centrosymmetric semiconductors, considerably expanding material choices for future sensing and energy applications. Here we report an experimental demonstration of the flexo-photovoltaic effect in an archetypal two-dimensional material, MoS_2, by using a strain-gradient engineering approach based on the structural inhomogeneity and phase transition of a hybrid system consisting of MoS_2 and VO_2. The experimental bulk photovoltaic coefficient in MoS_2 is orders of magnitude higher than that in most non-centrosymmetric materials. Our findings unveil the fundamental relation between the flexo-photovoltaic effect and a strain gradient in low-dimensional materials, which could potentially inspire the exploration of new optoelectronic phenomena in strain-gradient-engineered materials.

The phenomenon of the generation of current and voltage in materials under illumination is known as the photovoltaic (PV) effect. The PV effect can be caused by charge separation via internal electric field out of heterostructures that often consist of two or more material components. However, in non-centrosymmetric materials consisting of a single component, a photocurrent can be generated on homogeneous illumination in the absence of external fields and spatial inhomogeneity. This phenomenon is named the bulk PV (BPV) effect[1]. For BPV effect, the current density $\mathbf{j}$ is expressed as[1]:

$$j_i = \beta_{ilm} E_l E_m^* I, \tag{1}$$

where β_{ilm} is the BPV coefficient (a third-rank tensor), E_l and E_m^* are the light polarization unit vectors and I is the light intensity. Commonly, the absorption anisotropy is unimportant, and β_{ilm} can be formulated as[1]:

$$\beta_{ilm} = \alpha G_{ilm}, \tag{2}$$

where α is the absorption coefficient, while G_{ilm} is the Glass coefficient charactering the current excitation performance. In the 1970s, the BPV effect was observed in $LiNbO_3$ (LNO)[2], $BaTiO_3$ (BTO)[3], $Pb(Zr_xTi_{1-x})O_3$ (PZT)[4] and other piezoelectric and ferroelectric crystals[1]. Because the BPV effect may be free from the Shockley–Queisser limit and enhance the existing efficiency of optoelectronics, it has recently been revisited in many ferroelectric materials (for example, Fe-doped LNO (LNO:Fe)[5], PZT[6], $BiFeO_3$ (BFO)[7,8], BTO[9,10], Bi_2FeCrO_6 (BFCO)[11] and $[KNbO_3]_{1-x}[BaNi_{1/2}Nb_{1/2}O_{3-\delta}]_x$ (KBNNO)[12]), and other non-centrosymmetric materials (for example, layered perovskite-type halides (LPH)[13], organic crystals[14], Weyl semimetal TaAs[15] and WS_2 nanotubes[16]).

To explain the physics of the BPV effect, a rigorous microscopic theory was proposed in 1982 (ref. [17]) by Belinicher, Ivchenko and Sturman. In this theory, the total BPV current density $\mathbf{j}$ included two physically different contributions: shift and ballistic currents,

$$\mathbf{j} = \mathbf{j}_{sh} + \mathbf{j}_b. \tag{3}$$

The shift current $\mathbf{j}_{sh}$ is caused by the displacements of electrons in real space on quantum transitions (see Supplementary Discussion 1 for details). Figure 1a shows a microscopic schematic of the displacements of electron clouds when electrons undergo a light-induced interband excitation from the valence band (VB) (cyan clouds, e_{VB}) to the conduction band (CB) (orange clouds, e_{CB}) in non-centrosymmetric unit cells. The displacement of the electron cloud results in an effective shift vector $\overline{\mathbf{R}}$. The continuous optical pumping generates a shift current in the steady non-equilibrium state. On the other hand, the ballistic current $\mathbf{j}_b$ is caused by the asymmetric velocity (v) distributions in bands as a result of kinetic processes including momentum relaxation (10–10^3 fs), energy relaxation (10–10^2 ps) and recombination (below roughly 1 ns) (see Supplementary Discussion 1 for details). Figure 1b shows a microscopic schematic of the BPV effect for interband transitions. Both shift and ballistic currents originating from the $\overline{\mathbf{R}}$ and effective velocity $\overline{\mathbf{v}}$, respectively, contribute to the total BPV current density (note that the directions of $\overline{\mathbf{R}}$ and $\overline{\mathbf{v}}$ may not be the same). Here, for simplicity, only the contribution of optical excitation to shift current is sketched in Fig. 1a,b.

Inversion symmetry can be lifted by strain gradient. Thus, the BPV effect can also be manifested in centrosymmetric materials when coupled with the flexoelectric effect, which is termed the flexo-PV (FPV) effect[18]. The flexoelectric effect, that is, the coupling phenomenon between electric polarization and strain gradient, was first proposed by Mashkevich and Tolpygo[19] and phenomenologically formulated by Kogan[20]. Via strain gradient, a non-polar material can become polar. In the absence of external electric field, the flexoelectric effect (static), a response of polarization P_i to strain gradient η_{lmn}, is governed by the flexoelectric coefficient

$$\mu_{ilmn} = \frac{\partial P_i}{\partial \eta_{lmn}}, \tag{4}$$

where $\eta_{lmn} = \partial u_{mn}/\partial x_l$ (u_{mn} is the strain), u_{ilmn} is a fourth rank tensor and the flexoelectric effect is symmetry allowed in any material. From a microscopic view, flexoelectricity includes two contributions: a lattice contribution due to internal atomic displacements

[1]Department of Materials Science and Engineering, Rensselaer Polytechnic Institute, Troy, NY, USA. [2]Department of Physics, Applied Physics and Astronomy, Rensselaer Polytechnic Institute, Troy, NY, USA. ✉e-mail: jiangj2@rpi.edu; shij4@rpi.edu

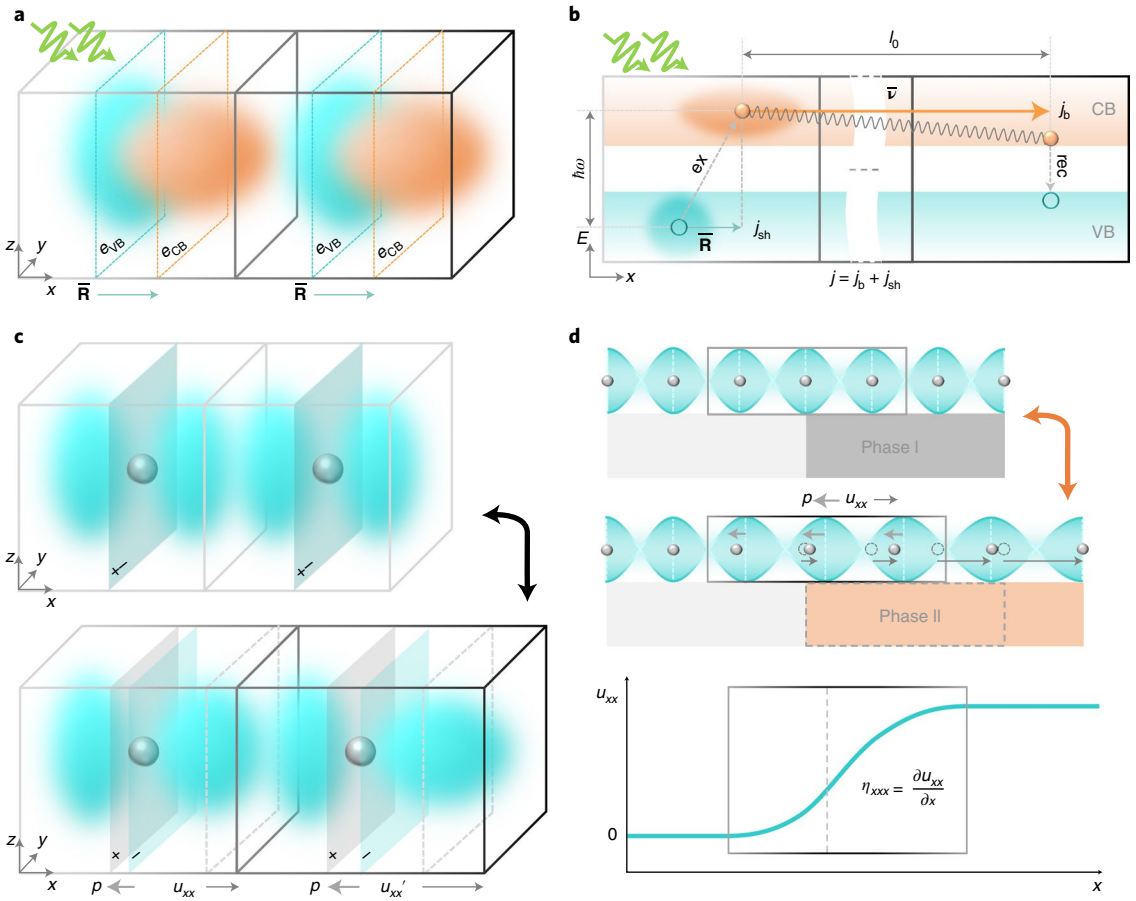

Fig. 1 | Microscopic views of the BPV and flexoelectric effects. a, Schematic of mechanism of shift current in real space on light-induced interband excitation. In non-centrosymmetric unit cells, the displacement of the electron cloud when electrons are excited from the valence band (cyan clouds, e_{VB}) to the conduction band (orange clouds, e_{VB}) yields a shift current. **b**, Schematic of mechanism of BPV current (including shift and ballistic currents) with lattice *x* on the horizontal axis and energy *E* on the vertical during excitation (ex), scattering and recombination (rec). For simplicity, only the contribution of optical excitation to shift current is sketched. $\bar{\mathbf{R}}$ and $\bar{\mathbf{v}}$ yield a shift current and a ballistic current, respectively. ℓ_0 is the free-path length of photo-excited hot electrons (holes). **c**, Electron cloud (p_x orbitals) distributions without (upper panel) and with (bottom panel) a strain gradient (strains u_{xx} and u'_{xx}, grey arrows). Electron redistribution shifts the negative charge centre (on the light cyan plane) away from the positive charge centre (on the light grey plane) along *x*, leading to a negative dipole moment *p* (bold grey arrow) in each unit cell. **d**, Strain-gradient engineering of a 2D material by using a phase-change material in a hybrid system. On a reversible structural phase transition between phase I (grey, upper panel) and phase II (orange, middle panel), strain gradients (increasing strains u_{xx}, grey arrows) are generated in the 2D material at the edge of the phase-change material (grey rectangular region, middle panel), inducing shifts of electron charge centres (electron wave function of *s* orbitals in cyan curves) and thereby dipole moments (bold grey arrows). Light grey rectangles represent the non-phase-change material. The strain plot (bottom panel) illustrates strain gradients in the 2D material.

based on a rigid-ion model and an electronic contribution due to charge-density redistributions induced by atomic displacements[21]. In illustrating the microscopic mechanism of flexoelectricity, the commonly used ionic pictures[22], with rigid ions shifting causing polarization under a strain gradient ignore the more fundamental electronic distribution. Here, we illustrate the electronic (frozen-ion) contribution in Fig. 1c. A simple model of one atom/unit cell (upper panel) is used and a positive strain gradient is applied along *x* (bottom panel). With the ion (grey ball) position fixed, p_x orbital deforms from a symmetric shape with zero dipole moment for each unit cell to an asymmetric structure leading to a negative dipole moment (grey arrows). Here the use of p_x orbital is for simplicity that does not lose the generality.

The flexoelectric effect is generally negligible in bulk crystals mainly due to the small strain (roughly 10^{-6}) and strain gradient (roughly 0.1 m^{-1}) often induced by mechanical bending[23]. However, giant strain gradients have been found at phase boundaries (roughly 10^7 m^{-1})[24], dislocation cores (roughly 10^9 m^{-1})[25] and crack tips (roughly 10^8 m^{-1})[26], in epitaxial thin films (roughly 10^6 m^{-1})[27] and generated by nano-indentation in ultrathin films (roughly 10^7 m^{-1})[28]. Recently, the flexoelectric effect induced by nano-indentation on crystals[18] and mechanical bending on freestanding films[29] coupled with the FPV effect has been reported. The existence of the large strain[30] in two-dimensional (2D) materials makes them fertile for exploring possible giant strain-gradient effects. Theoretically, the flexoelectric effect has been predicted in highly curved carbon nanoshells[31], boron nitride bilayers[32] and monolayer transition metal dichalcogenides[33]. Strain engineering in transition metal dichalcogenides has been designed[34,35] and experimentally reported[36] for potential applications in optoelectronics and PVs. However, the experimental study on strain-gradient engineering resulting in the FPV effect in 2D materials had not yet been achieved.

Here, we propose a unique strategy to generate and tune strain gradients in a 2D material. Our design is illustrated in Fig. 1d. In this design (top and middle panels), a 2D material (cyan object, one atomic layer is used to illustrate the design clearly) partially sits above a phase-change material (grey or orange rectangle) and partially above a non-phase-change material (light grey rectangle).

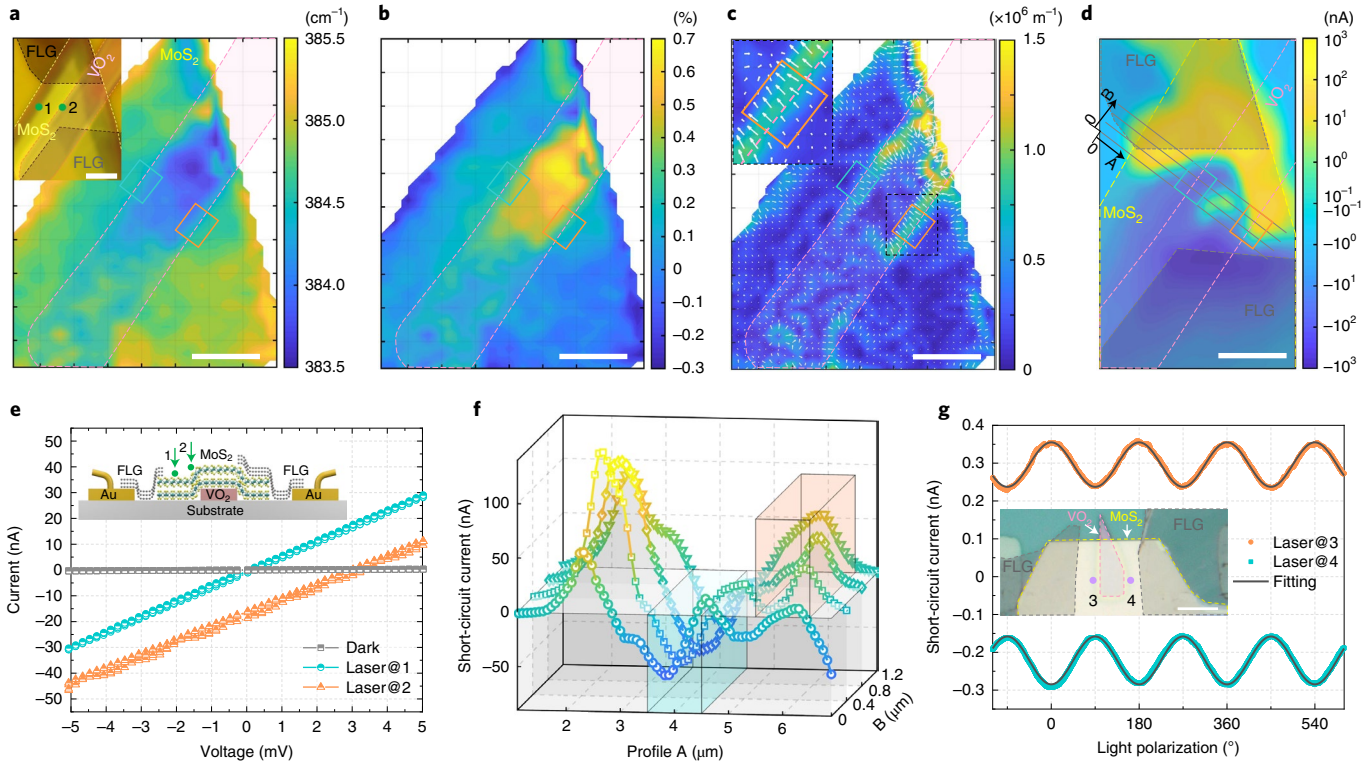

Fig. 2 | FPV effect of the MoS_2 sheet at room temperature. a, Raman mapping of E^1_{2g} mode of MoS_2 on a device (no. 1) consisting of a thin MoS_2 sheet lying on a VO_2 microbeam and two FLGs as contacts. The inset shows an optical image (mapping area) of this device. **b**, Strain map of the MoS_2 sheet calculated from **a**. **c**, Map of strain-gradient value (colour) and vector (arrows) in the MoS_2 sheet calculated from **b**. Maximum strain gradients in the MoS_2 sheet are located at both edges of the microbeam with opposite directions. The inset is an enlarged view of the black dashed rectangle. **d**, Short-circuit photocurrent map of the device measured under illumination by a 532-nm laser. **e**, Current–voltage curves of the device under laser (532 nm) illumination at spot 1 (Laser@1) and 2 (Laser@2) and without illumination (Dark). The inset shows a schematic of the cross-sectional view of the device. The laser spots 1 and 2 are indicated by green dots in insets of **a** and **e**. **f**, Short-circuit photocurrent profiles A extracted from grey lines in **d**. Light cyan and light orange cuboids correspond to cyan and orange rectangles at both edges of the microbeam in **a**–**d**, respectively. **g**, Light polarization dependence of the short-circuit photocurrent under laser (405 nm) illumination at spots 3 (Laser@3) and 4 (Laser@4) in a device (no. 3). The inset shows an optical image of device no. 3. The dark grey curves are fitting ones. Shapes/boundaries of the MoS_2 sheet, VO_2 microbeam and FLGs are outlined in yellow, pink and grey dashed lines, respectively, in **a**–**d** and inset of **g**. The region of the microbeam is painted in light pink in **a**–**d** and inset of **g**. The colour code scales in **a**–**d** indicate the values of the relevant parameters with their corresponding units shown alongside. Scale bars in **a**–**d**, 2 μm; inset of **g**, 10 μm.

The structural phase transition (between grey phase I and orange phase II) of the phase-change material can be controlled by external stimuli (for example, temperature or electric field). We then expect such a phase transition to induce strains (shifts of atoms, grey arrows) and strain gradients (highlighted by solid rectangular box) in the 2D material. Particularly, right above phase II, a uniform strain is expected; near the boundary between the phase-change material and non-phase-change material, a strain gradient is expected, as illustrated in the bottom panel. These strain gradients would tune the electron-density distribution (illustrated as cyan waves with *s* orbital), leading to non-zero dipole moments along the strain-gradient direction (bold grey arrows), that is, flexoelectricity. The lifting of inversion symmetry by flexoelectricity via our strain-gradient engineering approach and the existence of extraordinary optoelectronic properties in 2D materials make it possible to explore 2D materials' FPV effect.

FPV effect in MoS_2 sheets

In the present study, we choose VO_2 as a representative phase-change material to achieve strain-gradient engineering and reveal the FPV effect in a representative 2D material MoS_2 (see the atomic schematics in Supplementary Fig. 1a–g and the description in Supplementary Discussion 2). By using a typical transfer technique (all-dry viscoelastic stamping) that is widely used in the 2D community[37], we have fabricated a device (no. 1) consisting of a thin MoS_2 sheet on a VO_2 microbeam (25 μm × 2 μm × 118 nm) and two few-layer graphene (FLG) as contacts (see the optical image in Supplementary Fig. 2 and detailed descriptions of the device fabrication in Methods). The thickness of the microbeam (roughly 118 nm), MoS_2 sheet (roughly 16 layers for the region at the left edge of the microbeam) and FLGs are characterized by atomic force microscopy (Supplementary Fig. 3a–h). The structures of both the MoS_2 sheet and FLG are studied by confocal Raman measurements (a representative Raman spectrum and mappings of FLG and MoS_2 in Supplementary Fig. 4a–c, respectively). Specifically, Supplementary Fig. 5b shows Raman spectra of the E^1_{2g} mode of MoS_2 measured at laser spots 1–6 in Supplementary Fig. 5a. Remarkable red shifts of the E^1_{2g} mode are observed for the laser spots 3–6, indicating a tensile strain and a strain gradient in the regions of the MoS_2 sheet at the surface and edge of the microbeam, respectively. Figure 2a shows a complete Raman mapping of E^1_{2g} mode of MoS_2 with a mapping area shown in its inset optical image. On the basis of the shift of E^1_{2g} mode with respect to uniaxial strain reported from literature for few-layer MoS_2 (−1.7 cm^{-1} per percentage of strain[38]), with the region of the MoS_2 sheet far away from the microbeam as a reference (the E^1_{2g} mode is nearly constant when the layer number is above four[39] and here it is at 384.9 cm^{-1}), strains and

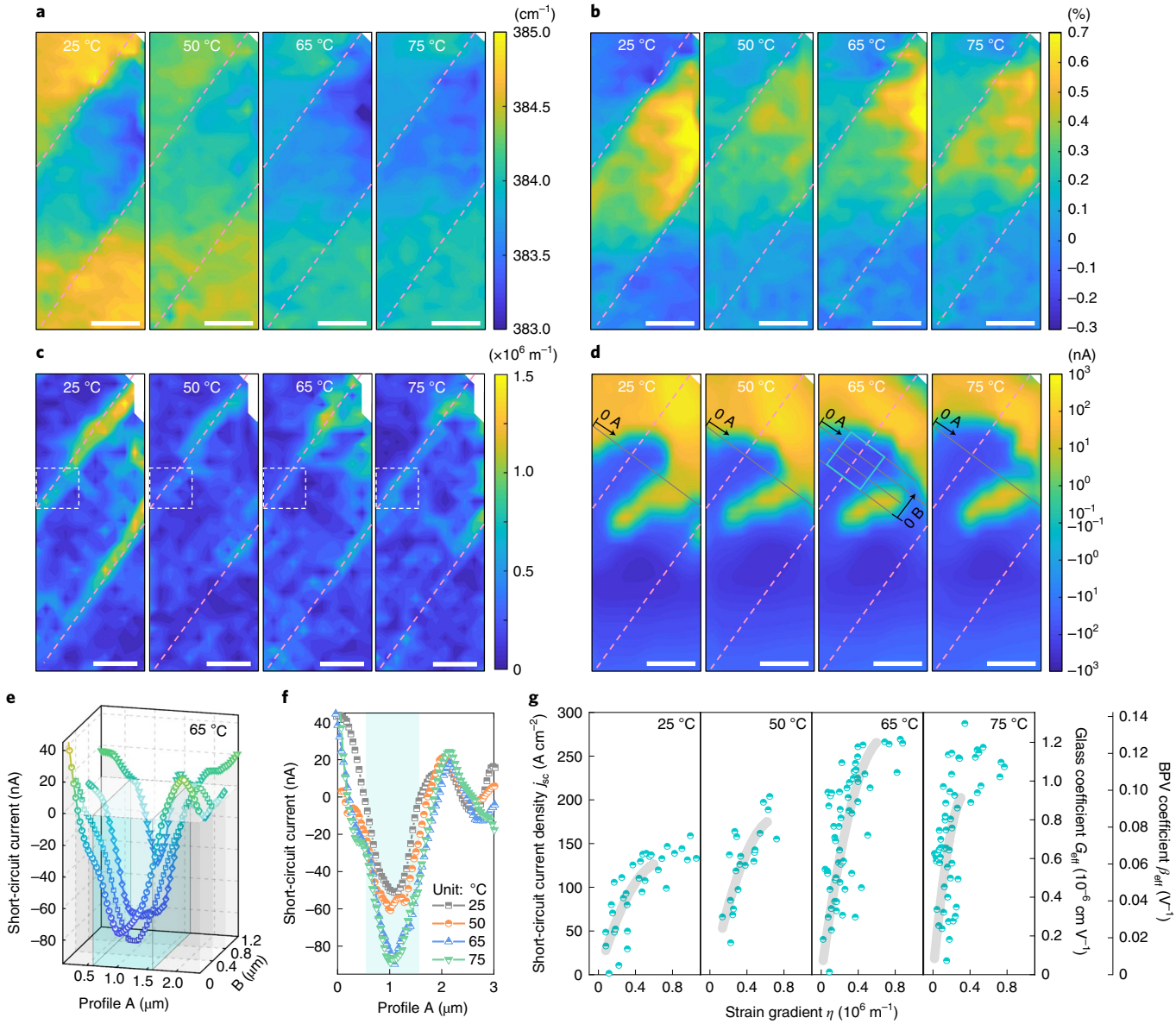

Fig. 3 | Temperature-dependent FPV effect of the MoS_2 sheet. a, Raman mappings of E^1_{2g} mode of MoS_2 on device no. 1 at 25–75 °C. **b**, Strain maps of the MoS_2 sheet at 25–75 °C calculated from **a**. **c**, Maps of strain-gradient value in the MoS_2 sheet at 25–75 °C calculated from **b**. **d**, Short-circuit photocurrent maps of the device at 25–75 °C. Edges of the microbeam are outlined in pink dashed lines in **a**–**d**. **e**, Short-circuit photocurrent profiles A extracted from grey lines perpendicularly crossing the VO_2 microbeam in **d** at 65 °C. The light cyan cuboid corresponds to the cyan rectangle in **d**. **f**, Short-circuit photocurrent profiles A extracted from grey lines in **d** at 25–75 °C. Enhancements of current peaks (absolute values) at 65 and 75 °C compared with those at 25 and 50 °C suggest a tuning of the FPV effect in the MoS_2 sheet by the phase transition of the microbeam. **g**, Plots of short-circuit current density j_{sc} (left axis) versus strain gradient η. η and j_{sc} are extracted from the data in the white dashed rectangles in **c** and corresponding regions in **d**, respectively. Only effective data points (with negative currents) are plotted. The calculated effective Glass coefficient G_{eff} and BPV coefficient β_{eff} are shown on the right axes. Light grey curves are guides to the eye. The colour code scales in **a**–**d** indicate the values of the relevant parameters, with their corresponding units shown alongside. Scale bars in **a**–**d**, 1 μm.

strain gradients (value in colour and vector in arrow) in the MoS_2 sheet can be calculated and are mapped in Fig. 2b,c, respectively. The MoS_2 sheet has tensile strains (up to 0.7%) in the region at the surface of the microbeam and maximum strain gradients (exceeds 10^6 m^{-1}) with opposite directions in the region at both edges of the microbeam (see an enlarged view of the right edge in the inset of Fig. 2c). It should be mentioned that the 'strain gradients' and 'negative strains' at the edge of the MoS_2 sheet could be artefacts because monolayer exists at the edge (Supplementary Fig. 3b,d) and its E^1_{2g} mode is lower than that of few-layer MoS_2 (ref. [38]).

To study the FPV effect, we use scanning photocurrent microscopy (SPCM) to map photocurrents across the whole device (Fig. 2d). At the regions with small (spot 1) and large (spot 2) strain gradients (marked in green dots in both insets of Fig. 2a,e), we measure current–voltage curves with (Laser@1 and Laser@2) and without illumination (Dark) for comparison, as shown in Fig. 2e (corresponding curves in the logarithmic scale and photo responses are shown in Supplementary Fig. 6a,b, respectively). A large short-circuit photocurrent is observed at spot 2. The short-circuit photocurrents (Fig. 2d) with opposite signs are observed in regions on FLGs

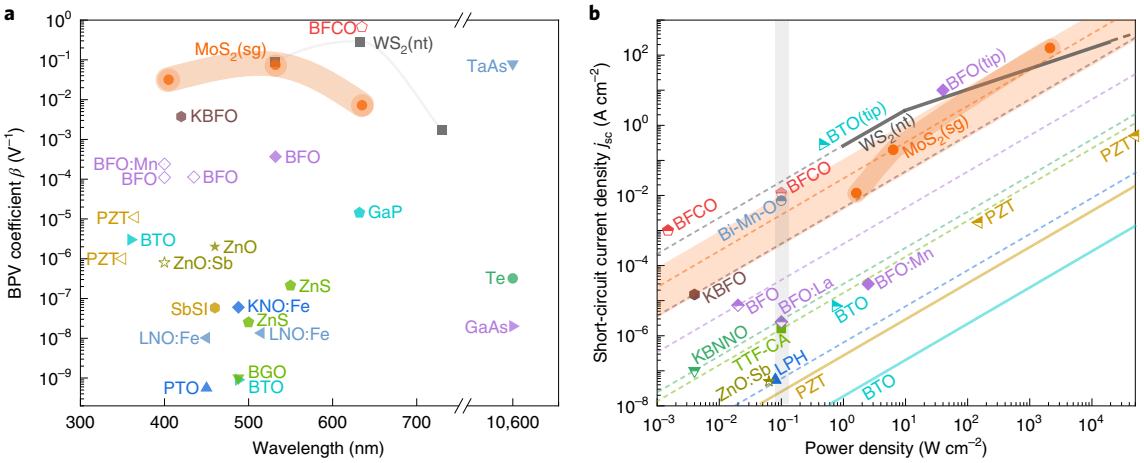

Fig. 4 | Overview of the BPV effect in non-centrosymmetric materials. a, Experimental BPV coefficients β for non-centrosymmetric materials. Data for bulk materials (WS_2 nanotube (nt)[16], TaAs[15], KBFO[52], BFO[7], GaP[53], ZnO[54], Te[1], ZnS[1], Fe-doped $KNbO_3$ (KNO:Fe)[1], SbSI[55], GaAs[1], LNO:Fe[5], $Bi_{12}GeO_{20}$ (BGO)[56], BTO[1], $PbTiO_3$ (PTO)[1]) and thin films (BFCO[11], Mn-doped BFO (BFO:Mn)[57], BFO[57], PZT[47], BTO[9], Sb-doped ZnO (ZnO:Sb)[58]) are shown as solid and open symbols, respectively. Data for BTO and ZnO are β_{31}, for Te, LNO:Fe and BFO:Mn are β_{33}, for BFO is β_{22}, for BGO are β_{14}, and for others are effective values. All data are from the linear BPV effect. **b**, Short-circuit current density j_{sc} versus incident power density in reported non-centrosymmetric materials. Data for materials with solid symbols (BFO with a tip enhancement (BFO(tip))[8], KBFO[52], tetrathiafulvalene-*p*-chloranil (TTF-CA)[14], BFO:Mn[57], LPH[13]) and solid lines are for the lateral configuration, while half-filled symbols (BFCO[11], Bi-Mn-O composite thin film[59], BTO with a tip enhancement (BTO(tip))[10], BFO[7], KBNNO[12], La-substituted BFO (BFO:La)[60], BTO[9], PZT[47], ZnO:Sb[58]) are for the vertical configuration. The solid grey line for WS_2(nt) is drawn from the values in ref. [16]. The solid yellow and cyan lines for PZT and BTO, respectively, are drawn from the values in ref. [4]. Parallel dashed colour lines are linear expansions of data for bulk materials (others are for thin films) based on equation (1). Data for materials in the light grey shadow are measured under AM 1.5 G radiation (0.1 W cm^{-2}), while others are measured by light sources with specific wavelengths (expect for KBNNO by a halogen lamp[12]). Our results for strain-gradient-engineered MoS_2 (MoS_2(sg)) are shown as orange circles highlighted by the light orange shadow in both **a** and **b**. Illuminations of 405, 532 and 635 nm are at power densities of 6.32, 2.11 and 1.61 W cm^{-2}, respectively.

(upper yellow and bottom blue, possibly as a result of the existence of a double Schottky diode[16] and the photothermoelectric effect[40]) and at both edges of the VO_2 microbeam. Specifically, short-circuit photocurrent profiles along grey lines perpendicularly crossing the microbeam are extracted and plotted in Fig. 2f. The light cyan and light orange cuboids in Fig. 2f correspond to the cyan and orange rectangles at both edges of the microbeam in Fig. 2d, respectively. The current peaks with opposite signs are located at both edges of the microbeam (giant strain gradients are found in these two locations). These microbeam-edge currents could be explained by the FPV effect (details are presented in later paragraphs).

The origin of positive current peaks at around 5 μm of profile A in Fig. 2f (corresponding to the positive-current region at the middle of the microbeam in Fig. 2d) is not clear and may be related to a build-in field manifested at the interface between MoS_2 and VO_2. The potential gradient due to charge transfer/band bending in the lateral direction across the microbeam edge, if it exists, may induce a built-in field, resulting in a short-circuit photocurrent. To rule out this, we have designed and conducted a control experiment in which a VO_2 microbeam is stacked on the MoS_2 sheet to avoid forming strain gradient but keep the interface of MoS_2–VO_2 (see Supplementary Fig. 7a–d and Supplementary Discussion 3 for more details). According to our experiment, the contribution from this is negligible.

To improve statistics, we have fabricated and tested five more devices with different thicknesses of MoS_2 sheets and VO_2 microbeams (device nos. 2–6; see Supplementary Figs. 8a–j, 9a–j, 10a–j, 11a–g, 12a–h and 13a,b and Supplementary Discussion 4 for more details). Despite different thicknesses and uniformity of the MoS_2 sheets among all devices, the experimental observations of strain gradient and its relation to photocurrents are similar.

On the basis of equation (1), the light polarization dependence of short-circuit photocurrent is one important piece of evidence to support the BPV effect, which is inherited by the FPV effect[18]. For the case of a centrosymmetric structure with a strain gradient (here, the strain-gradient-engineered MoS_2), this dependence can be described as

$$j_3^{\mathrm{L}} = \left(\beta_{311}\sin(\theta)^2 + \beta_{333}\cos(\theta)^2\right) I, \quad (5)$$

where j_3^{L} is the component along the polar axis of the sample (the direction of the strain gradient) of the linearly polarized light-induced BPV current density j_i^{L}, β_{311} and β_{333} are the linear BPV tensor β_{ilm}^{L} elements and θ is the angle between the polarization direction of the light and the direction of the strain gradient (see detailed analysis of β_{ilm}^{L} and j_i^{L} in Supplementary Fig. 14 and Supplementary Discussion 5). Thus, the FPV effect in the present case should exhibit a sinusoidal curve with a period of 180°. Indeed, a nearly perfect light polarization dependence can be found in our measured photocurrents in device no. 3 (inset of Fig. 2g) under laser (405 nm) illumination at both edges of the VO_2 microbeam, spots 3 and 4, as shown in Fig. 2g and Supplementary Fig. 15a–e (a 635-nm laser is used for Supplementary Fig. 15d,e). The theoretical fittings in Fig. 2g yield β_{333} of 8.1×10^{-2} and $6.5\times10^{-2}\,V^{-1}$, and β_{311} of 5.4×10^{-3} and $3.6\times10^{-3}\,V^{-1}$ for the upper curve and lower curve, respectively (corresponding strain gradients of roughly 2.5×10^{5} and $2.1\times10^{5}\,m^{-1}$, respectively). Similar phenomena can be found in other devices (Supplementary Fig. 16a,b for device nos. 2 and 6, respectively). The measurement setup and the calibration of the setup for polarization dependence are presented in Supplementary Fig. 17a–e. Our experimental results on light polarization dependence provide another set of evidence for the FPV effect in MoS_2.

The strain gradient of the MoS_2 sheet can be tuned by the temperature-induced structural phase transition of the VO_2 microbeam. Figure 3a shows Raman mappings of E_{2g}^1 mode at 25, 50, 65 and 75 °C (after the sample experiences a cycle of heating

and cooling). This 25 °C result is largely consistent with the one before the heating and cooling cycle (Fig. 2a), indicating the reproducibility and phase transition reversibility. A slight red shift of E^1_{2g} mode of MoS_2 in the region without the microbeam underneath (the microbeam is outlined in pink dashed lines) with increasing temperature is observed. Such a shift stems from thermal expansion and the temperature-induced anharmonicity of lattice vibration[41]. With the region of the MoS_2 sheet far away from the microbeam as a reference (that is, E^1_{2g} mode of 384.4 cm^{-1} at 50 °C, 384.0 cm^{-1} at 65 °C and 383.9 cm^{-1} at 75 °C), strains and strain-gradient values in the MoS_2 sheet at 25–75 °C (white dashed rectangular regions in Supplementary Fig. 18a–d) are calculated from Fig. 3a and mapped in Fig. 3b,c, respectively. Note that selecting a different reference would not change the values and directions of strain gradients, although strain values could vary. Since the FPV effects are only dependent on strain gradients, having an arbitrary reference would not change our conclusion. In Fig. 3b, pristine tensile strains at 25 °C in the region of the MoS_2 sheet on the microbeam, which are formed as a consequence of the microbeam geometry, are reduced when the temperature reaches 50 °C. Since MoS_2 has a larger thermal expansion coefficient of $1.9\times10^{-6}\,K^{-1}$ (in plane)[42] than the substrate (for example, for SiO_2 $5\times10^{-7}\,K^{-1}$)[43], the reduction of pristine tensile strains can thus be explained by the substrate clamping effect. This can further explain the observed reduced strain gradients at both edges of the microbeam at 50 °C (Fig. 3c). When the temperature reaches 65 °C, the structural phase transition of the microbeam occurs. This can be seen by the slight contrast change of R-phase VO_2 domains in the optical images in Supplementary Fig. 18c,d (small and large domains at 65 and 75 °C, respectively). The structural phase transition (from M1 to R) of the microbeam is also confirmed by the disappearance of A_g modes of VO_2 in Raman spectra (Supplementary Fig. 18e). Across the phase transition, along both in-plane and out-of-plane radial-axis directions of the microbeam (that is, the axes perpendicular to $(0\bar{1}1)$ and (011) of M1-phase VO_2 (ref. [44]), respectively), there exist sudden elongations of the VO_2 lattice (that is, 0.3% along both directions illustrated in Supplementary Fig. 1e–g). These elongations in the microbeam could stretch the MoS_2 sheet right on top, which could further lead to increased tensile strains and thus larger strain gradients at the edge of the microbeam. Indeed, we have observed the enhanced tensile strains (Fig. 3b) and strain gradients (Fig. 3c) in the MoS_2 sheet after the phase transition of the microbeam at 65 °C compared with 50 °C. At 75 °C (compared with 65 °C), the observed reduction of the tensile strains and the corresponding strain gradients (slightly reduced) in the MoS_2 sheet at the surface and edge of the microbeam, respectively, can be attributed to the same substrate clamping effect observed from 25 to 50 °C.

Figure 3d shows short-circuit photocurrent maps at 25–75 °C measured at the same region as Fig. 3a–c for each temperature. For all temperatures, we find that photocurrent peaks and strain-gradient peaks in the MoS_2 sheet appear at same locations. Figure 3e shows extracted current profiles along grey lines perpendicularly crossing the VO_2 microbeam at 65 °C in Fig. 3d. By comparing current profiles at different temperatures in Fig. 3f extracted from Fig. 3d, we can see that at 65 and 75 °C around the 1 μm position, the photocurrents are substantially higher than those at 25 and 50 °C (absolute values). Parameters such as contact resistance, carrier mobility or charge diffusion length or carrier lifetime[45] may lead to different photocurrents at different temperatures. In this study, we can receive the net contribution of temperature on the photocurrent by investigating the regions that do not have substantial strain gradient. In these regions, the lack of strain gradient rules out the contribution of photocurrent from FPV effect so we can focus on the net contribution of temperature-dependent contact resistance, carrier mobility and other factors. In the region with small strain gradients (along profile Y in light grey in Supplementary Fig. 19a,b), we find that the photocurrent is reduced (absolute value) at increased temperature. This observation indicates that the reduced contact resistance is not significant enough to counter the possible reduction of light-current conversion efficiency due to the possible suppression of carrier mobility or diffusion length or carrier lifetime. In the large strain-gradient region, the temperature-dependent short-circuit photocurrent shows an enhancement (absolute value) at or above 65 °C rather than reduction in the light grey region along profile Y. These observations show that the net contribution of increasing temperature on the light-current conversion efficiency as a result of temperature-dependent contact resistance change, temperature-dependent mobility change and so on, is negative rather than positive. These observations confirm the role of strain-gradient engineering by the phase transition of the microbeam on the FPV effect of the MoS_2 sheet. Similar FPV effect engineering has been also achieved in other devices (for example, Supplementary Figs. 20a–d and 21a–d for device nos. 2 and 3, respectively).

By extracting strain gradients in the white dashed rectangles in Fig. 3c (away from the contact region to eliminate the influence of FLG/MoS_2 contact) and the corresponding short-circuit photocurrents in Fig. 3d, the short-circuit current density j_{sc} values versus strain gradients η at 25–75 °C are plotted in Fig. 3g. Here, the cross-sectional area of the MoS_2 sheet at the interface of FLG and MoS_2 is chosen as the contact area for device no. 1, which is computed to be $3.2\times10^{-10}\,cm^2$. Clearly, both maximum values of η and j_{sc} at 65 °C and 75 °C are much higher than those at 50 °C. It is also noticed that the relationship between j_{sc} and η is non-linear. The demonstration of enhancement of strain gradient and photocurrent across the phase transition temperature suggests the effectiveness of structural phase transition on tuning FPV effect. Since voltage can drive phase transition of VO_2, it is possible to design devices in future in which the FPV effect is tuned electrically, which would open a new window in controlling light–matter interactions.

BPV coefficient

To quantify the observed phenomena in terms of the BPV effect in our strain-gradient-engineered MoS_2 sheets, we evaluate the Glass coefficient G and BPV coefficient β on the basis of the measured photocurrents. According to equations (1) and (2), the absorption coefficient of MoS_2 ($2.74\times10^5\,cm^{-1}$ at 532 nm, ref. [46]), the effective G_{eff} and β_{eff} of the MoS_2 sheet in device no. 1 are calculated for 25–75 °C (right vertical axes of Fig. 3g). Here, we calculate effective values of the linear BPV tensor β^L_{ilm} due to the irregular geometry of the device (inset of Fig. 2a). The maximum G_{eff} and β_{eff} are greatly enhanced by the phase transition of VO_2 (above 65 °C, up to $4.36\pm0.31\times10^{-7}\,cm\,V^{-1}$ and $0.12\pm0.01\,V^{-1}$ at 75 °C, respectively), as shown in Supplementary Fig. 22.

Finally, we compare the BPV effect in the strain-gradient-engineered MoS_2 sheet with that in other non-centrosymmetric materials with values of Glass coefficient G and BPV coefficient β as two metric parameters. Our results (orange circles highlighted by light orange shadows at 405, 532 and 635 nm obtained from device nos. 2, 1 and 3, respectively) are plotted alongside G and β of other materials in Supplementary Figs. 23 and Fig. 4a, respectively. By taking the absorption coefficient into account, β_{eff} in the strain-gradient-engineered MoS_2 sheet is orders of magnitude larger than most reported values of other materials in the visible range (except for BFCO[11] and WS_2 nanotubes[16]).

Meanwhile, short-circuit current density j_{sc} values for reported materials are plotted against the illumination power density in Fig. 4b. The performance of the PV effect does not only depend on material properties, but also relies on other parameters, for example thickness[9,47], buffer layer[48], tip enhancement[8,10], Schottky barrier[49], domain wall[50] and device geometry[51]. Figure 4b presents the reported j_{sc} for both lateral (solid lines and solid symbols) and vertical (half-filled symbols) devices. Among these lateral devices,

in terms of j_{sc}, our MoS_2 sheet is comparable with WS_2 nanotubes[16] and is orders of magnitude larger than other materials. Typically, in a lateral device, if the spacing between electrodes is much longer than the charge diffusion length, its j_{sc} would be much lower than a vertical device with the thickness of the active layer closer to the charge diffusion length[51]. Therefore, the performance of the strain-gradient-engineered MoS_2 sheet could be further enhanced by using the vertical device configuration.

Conclusion

In summary, with a unique strain-gradient engineering approach, we have discovered the FPV effect in a centrosymmetric 2D material MoS_2. With the temperature-induced structural phase transition of the VO_2 microbeam in the hybrid system, the MoS_2 sheet could carry giant strain gradients of up to $10^6\,m^{-1}$. Compared to most non-centrosymmetric insulators and semiconductors, our strain-gradient-engineered MoS_2 sheet carries orders of magnitude higher Glass and BPV coefficients, probably due to the accessibility of giant strain gradient and the intrinsic superior optoelectronic property in MoS_2. Our discovery of the FPV effect in the 2D material enriches the basic understanding of the FPV effect and may enable new concepts and materials for potential PV applications.

Online content

Any methods, additional references, Nature Research reporting summaries, source data, extended data, supplementary information, acknowledgements, peer review information; details of author contributions and competing interests; and statements of data and code availability are available at https://doi.org/10.1038/s41565-021-00919-y.

Received: 21 September 2020; Accepted: 27 April 2021;
Published online: 17 June 2021

References

1. Sturman, B. I. & Fridkin, V. M. *Photovoltaic and Photo-Refractive Effects in Noncentrosymmetric Materials* Vol. 8 (CRC, 1992).
2. Glass, A. M., Linde, D. V. D. & Negran, T. J. High-voltage bulk photovoltaic effect and the photorefractive process in $LiNbO_3$. *Appl. Phys. Lett.* **25**, 233–235 (1974).
3. Koch, W. T. H., Munser, R., Ruppel, W. & Würfel, P. Bulk photovoltaic effect in $BaTiO_3$. *Solid State Commun.* **17**, 847–850 (1975).
4. Brody, P. S. High voltage photovoltaic effect in barium titanate and lead titanate-lead zirconate ceramics. *J. Solid State Chem.* **12**, 193–200 (1975).
5. Nadupalli, S., Kreisel, J. & Granzow, T. Increasing bulk photovoltaic current by strain tuning. *Sci. Adv.* **5**, eaau9199 (2019).
6. Qin, M., Yao, K. & Liang, Y. C. High efficient photovoltaics in nanoscaled ferroelectric thin films. *Appl. Phys. Lett.* **93**, 122904 (2008).
7. Choi, T., Lee, S., Choi, Y. J., Kiryukhin, V. & Cheong, S.-W. Switchable ferroelectric diode and photovoltaic effect in $BiFeO_3$. *Science* **324**, 63–66 (2009).
8. Alexe, M. & Hesse, D. Tip-enhanced photovoltaic effects in bismuth ferrite. *Nat. Commun.* **2**, 256 (2011).
9. Zenkevich, A. et al. Giant bulk photovoltaic effect in thin ferroelectric $BaTiO_3$ films. *Phys. Rev. B* **90**, 161409 (2014).
10. Spanier, J. E. et al. Power conversion efficiency exceeding the Shockley–Queisser limit in a ferroelectric insulator. *Nat. Photonics* **10**, 611–616 (2016).
11. Nechache, R. et al. Photovoltaic properties of Bi_2FeCrO_6 epitaxial thin films. *Appl. Phys. Lett.* **98**, 202902 (2011).
12. Grinberg, I. et al. Perovskite oxides for visible-light-absorbing ferroelectric and photovoltaic materials. *Nature* **503**, 509–512 (2013).
13. Sun, Z. et al. A photoferroelectric perovskite-type organometallic halide with exceptional anisotropy of bulk photovoltaic effects. *Angew. Chem. Int. Ed.* **55**, 6545–6550 (2016).
14. Nakamura, M. et al. Shift current photovoltaic effect in a ferroelectric charge-transfer complex. *Nat. Commun.* **8**, 281 (2017).
15. Osterhoudt, G. B. et al. Colossal mid-infrared bulk photovoltaic effect in a type-I Weyl semimetal. *Nat. Mater.* **18**, 471–475 (2019).
16. Zhang, Y. J. et al. Enhanced intrinsic photovoltaic effect in tungsten disulfide nanotubes. *Nature* **570**, 349–353 (2019).
17. Belinicher, V., Ivchenko, E. & Sturman, B. Kinetic theory of the displacement photovoltaic effect in piezoelectrics. *Zh. Eksp. Teor. Fiz.* **83**, 649–661 (1982).
18. Yang, M.-M., Kim, D. J. & Alexe, M. Flexo-photovoltaic effect. *Science* **360**, 904–907 (2018).
19. Mashkevich, V. & Tolpygo, K. Electrical, optical and elastic properties of diamond type crystals. *Sov. Phys. JETP* **5**, 435–439 (1957).
20. Kogan, S. M. Piezoelectric effect during inhomogeneous deformation and acoustic scattering of carriers in crystals. *Sov. Phys. Solid State* **5**, 2069–2070 (1964).
21. Hong, J. & Vanderbilt, D. First-principles theory of frozen-ion flexoelectricity. *Phys. Rev. B* **84**, 180101 (2011).
22. Wang, B., Gu, Y., Zhang, S. & Chen, L.-Q. Flexoelectricity in solids: progress, challenges, and perspectives. *Prog. Mater. Sci.* **106**, 100570 (2019).
23. Cross, L. E. Flexoelectric effects: charge separation in insulating solids subjected to elastic strain gradients. *J. Mater. Sci.* **41**, 53–63 (2006).
24. Chu, K. et al. Enhancement of the anisotropic photocurrent in ferroelectric oxides by strain gradients. *Nat. Nanotechnol.* **10**, 972–979 (2015).
25. Gao, P. et al. Atomic-scale measurement of flexoelectric polarization at $SrTiO_3$ dislocations. *Phys. Rev. Lett.* **120**, 267601 (2018).
26. Wang, H. et al. Direct observation of huge flexoelectric polarization around crack tips. *Nano Lett.* **20**, 88–94 (2020).
27. Lee, D. et al. Giant flexoelectric effect in ferroelectric epitaxial thin films. *Phys. Rev. Lett.* **107**, 057602 (2011).
28. Park, S. M. et al. Colossal flexoresistance in dielectrics. *Nat. Commun.* **11**, 2586 (2020).
29. Guo, R. et al. Continuously controllable photoconductance in freestanding $BiFeO_3$ by the macroscopic flexoelectric effect. *Nat. Commun.* **11**, 2571 (2020).
30. Bertolazzi, S., Brivio, J. & Kis, A. Stretching and breaking of ultrathin MoS_2. *ACS Nano* **5**, 9703–9709 (2011).
31. Dumitrică, T., Landis, C. M. & Yakobson, B. I. Curvature-induced polarization in carbon nanoshells. *Chem. Phys. Lett.* **360**, 182–188 (2002).
32. Duerloo, K.-A. N. & Reed, E. J. Flexural electromechanical coupling: a nanoscale emergent property of boron nitride bilayers. *Nano Lett.* **13**, 1681–1686 (2013).
33. Shi, W., Guo, Y., Zhang, Z. & Guo, W. Flexoelectricity in monolayer transition metal dichalcogenides. *J. Phys. Chem. Lett.* **9**, 6841–6846 (2018).
34. Feng, J., Qian, X. F., Huang, C. W. & Li, J. Strain-engineered artificial atom as a broad-spectrum solar energy funnel. *Nat. Photonics* **6**, 865–871 (2012).
35. Schankler, A. M., Gao, L. & Rappe, A. M. Large bulk piezophotovoltaic effect of monolayer 2H-MoS_2. *J. Phys. Chem. Lett.* **12**, 1244–1249 (2021).
36. Li, H. et al. Optoelectronic crystal of artificial atoms in strain-textured molybdenum disulphide. *Nat. Commun.* **6**, 7381 (2015).
37. Castellanos-Gomez, A. et al. Deterministic transfer of two-dimensional materials by all-dry viscoelastic stamping. *2D Mater.* **1**, 011002 (2014).
38. Rice, C. et al. Raman-scattering measurements and first-principles calculations of strain-induced phonon shifts in monolayer MoS_2. *Phys. Rev. B* **87**, 081307 (2013).
39. Chakraborty, B., Matte, H. S. S. R., Sood, A. K. & Rao, C. N. R. Layer-dependent resonant Raman scattering of a few layer MoS_2. *J. Raman Spectrosc.* **44**, 92–96 (2013).
40. Buscema, M. et al. Large and tunable photothermoelectric effect in single-layer MoS_2. *Nano Lett.* **13**, 358–363 (2013).
41. Sahoo, S., Gaur, A. P. S., Ahmadi, M., Guinel, M. J. F. & Katiyar, R. S. Temperature-dependent Raman studies and thermal conductivity of few-layer MoS_2. *J. Phys. Chem. C.* **117**, 9042–9047 (2013).
42. El-Mahalawy, S. H. & Evans, B. L. The thermal expansion of 2H-MoS_2, 2H-$MoSe_2$ and 2H-WSe_2 between 20 and 800 °C. *J. Appl. Crystallogr.* **9**, 403–406 (1976).
43. Lager, G. A., Jorgensen, J. D. & Rotella, F. J. Crystal structure and thermal expansion of α-quartz SiO_2 at low temperatures. *J. Appl. Phys.* **53**, 6751–6756 (1982).
44. Cao, J. et al. Extended mapping and exploration of the vanadium dioxide stress-temperature phase diagram. *Nano Lett.* **10**, 2667–2673 (2010).
45. Cui, X. et al. Multi-terminal transport measurements of MoS_2 using a van der Waals heterostructure device platform. *Nat. Nanotechnol.* **10**, 534–540 (2015).
46. Beal, A. R. & Hughes, H. P. Kramers-Kronig analysis of the reflectivity spectra of 2H-MoS_2, 2H-$MoSe_2$and 2H-$MoTe_2$. *J. Phys. C: Solid State Phys.* **12**, 881–890 (1979).
47. Ichiki, M. et al. Photovoltaic effect of lead lanthanum zirconate titanate in a layered film structure design. *Appl. Phys. Lett.* **84**, 395–397 (2004).
48. Cao, D. et al. High-efficiency ferroelectric-film solar cells with an n-type Cu_2O cathode buffer layer. *Nano Lett.* **12**, 2803–2809 (2012).
49. Ji, W., Yao, K. & Liang, Y. C. Bulk photovoltaic effect at visible wavelength in epitaxial ferroelectric $BiFeO_3$ thin films. *Adv. Mater.* **22**, 1763–1766 (2010).
50. Yang, S. Y. et al. Above-bandgap voltages from ferroelectric photovoltaic devices. *Nat. Nanotechnol.* **5**, 143–147 (2010).
51. Xiao, Z. et al. Giant switchable photovoltaic effect in organometal trihalide perovskite devices. *Nat. Mater.* **14**, 193–198 (2015).
52. Zhang, G. et al. New high *Tc* multiferroics $KBiFe_2O_5$ with narrow band gap and promising photovoltaic effect. *Sci. Rep.* **3**, 1265 (2013).

53. Astafiev, S., Fridkin, V. & Lazarev, V. The influence of the magnetic field on the linear bulk photovoltaic current in piezoelectric semiconductor GaP. *Ferroelectrics* **80**, 251–254 (1988).
54. Fridkin, V. M., Grekov, A. A. & Rodin, A. I. The bulk photovoltaic effect in the crystals without a center of symmetry. *Ferroelectrics* **43**, 99–108 (1982).
55. Mistewicz, K., Nowak, M. & Stróż, D. A ferroelectric–photovoltaic effect in SbSI nanowires. *Nanomaterials* **9**, 580 (2019).
56. Burger, A. M. et al. Direct observation of shift and ballistic photovoltaic currents. *Sci. Adv.* **5**, eaau5588 (2019).
57. Matsuo, H., Noguchi, Y. & Miyayama, M. Gap-state engineering of visible-light-active ferroelectrics for photovoltaic applications. *Nat. Commun.* **8**, 207 (2017).
58. Laurenti, M. et al. Nanobranched ZnO structure: p-type doping induces piezoelectric voltage generation and ferroelectric–photovoltaic effect. *Adv. Mater.* **27**, 4218–4223 (2015).
59. Chakrabartty, J., Harnagea, C., Celikin, M., Rosei, F. & Nechache, R. Improved photovoltaic performance from inorganic perovskite oxide thin films with mixed crystal phases. *Nat. Photonics* **12**, 271–276 (2018).
60. You, L. et al. Enhancing ferroelectric photovoltaic effect by polar order engineering. *Sci. Adv.* **4**, eaat3438 (2018).

Methods

Device fabrication. Maskless lithography (Intelligent Micro Patterning model SF-100 Lightning Plus, positive photoresist S1813) was used to draw patterns on a SiO_2 (roughly 300 or 1,000 nm)/Si(100) substrate with a channel distance of 20 μm. Then, Ti (3 nm)/Au (20 nm) layers were deposited by the e-beam evaporation, onto the photoresist-patterned substrate. The Ti/Au-patterned substrate was developed after a lift-off process.

VO_2 microbeams were grown by chemical vapour deposition on *r*-plane sapphire substrate (MTI Corporation). V_2O_5 powder (99%, Sigma-Aldrich) was used as precursor. Before deposition, oxygen/argon (20%/80%) was flowed into the chamber to maintain the pressure at 1 torr. During deposition, the temperature of the precursor was kept at 950 °C. VO_2 microbeams were formed on the substrate at about 5 cm away from the precursor. With a polydimethylsiloxane (PDMS) stamp being pressed on the as-grown sample and then released quickly, a few VO_2 microbeams were attached to the stamp surface. MoS_2 bulk crystals (2H phase, HQ Graphene Inc.) were put onto scotch tape and exfoliated several times. Then they were pressed on a PDMS stamp. After the scotch tape was slowly removed, some ultrathin MoS_2 sheets were transferred onto the PDMS stamp. FLG was prepared as electrical contacts in the same way as MoS_2.

PDMS stamps with VO_2 microbeams, MoS_2 sheets or FLG were loaded onto a three-axis micro manipulator. Then they were aligned to metal patterns under an optical microscope. Using the three-axis micro manipulator, we gently attached the samples (VO_2 microbeams, MoS_2 sheets or FLG) onto the desired positions and then carefully released the PDMS stamp. After that, the sheets were left on the substrate. In this way, we fabricated a device consisting of a MoS_2 sheet on a VO_2 microbeam with two FLGs as contacts. We did not use monolayer MoS_2 for the flexoelectricity study because the piezoelectricity in monolayer MoS_2 could contribute photocurrent that would complicate the analysis. Bilayer MoS_2 is an ideal candidate (centrosymmetric) to explore its flexoelectricity and FPV effect. However, stacking a bilayer MoS_2 on a VO_2 microbeam (thicknesses of roughly 100–200 nm in our devices) without crack formation has been found to be technically challenging. Thus, in the present study, we use a MoS_2 sheet with a thickness of roughly 10–100 nm to achieve the device fabrication on a VO_2 microbeam.

Characterizations. The morphology of the device was characterized by a Nikon Eclipse Ti-S inverted optical microscope. A multi-mode tapping mode atomic force microscope was used to measure the thickness of the MoS_2 sheet, VO_2 microbeam and FLGs with a tapping mode. Vibration modes of the MoS_2 sheet, VO_2 microbeam, FLGs and substrate were obtained from Raman spectra collected by using a WITec Alpha 300 confocal Raman microscope with an excitation source of a CW 532-nm laser. We use a ×100 objective lens for Raman measurements. A mapping mode with a step of 200 nm is used to map vibration modes of the MoS_2 sheet. Combining the confocal Raman microscope and a source meter (Keithley 2401), we built a SPCM machine to map the photocurrents in the device. Both Raman and photocurrent mappings are performed simultaneously. To avoid the laser heating that often results in the broadening and shifting of the Raman peaks and the possibility of damaging the sample, the laser power is adjusted to be as small as possible within the signal detection limit. Here, we use a laser power of about 8.6–1,000 μW for both Raman and photocurrent mappings. With these laser powers, the photothermoelectric-effect-induced current in the MoS_2 sheet could be neglected in the present study. For the light polarization dependence characterization, a 405-nm pulsed laser (type LDH-P-C-405, PicoQuant) (powers of 3.8 nW–48.4 μW are used), a 635-nm laser diode (LDM635, Thorlabs) with a filter (power of 108 nW) and an optical path including polarizer, quarter wave plate (WPQ10M-405 and AQWP10M-580, Thorlabs), dichroic or beam splitter and objective lens (×50) are used. A hand-held optical power/energy meter (Model 842-PE) is used to measure the laser power.

Data availability

The data of this study are available from the corresponding author upon reasonable request.

Acknowledgements

This work is supported by the US Army Research Office under grant number W911NF-21-1-0013 (J.J. and J.S.) and Air Force Office of Scientific Research under grant number FA9550-18-1-0116 (Y.W. and J.S.). The work is also supported by the NYSTAR Focus Center at Rensselaer Polytechnic Institute with contract number C150117 (L.Z., Y.X., G.-C.W. and J.S.). This work is also partially supported by the National Science Foundation under award numbers 2024972, 2031692 and 1916652 (Y.H., Z.C. and J.S.).

Author contributions

J.J. and J.S. conceived the idea and designed the experiments (device structure, temperature-dependent and photon-polarization-dependent measurements). J.J. built the 2D materials transfer system and assembled the SPCM setup. J.J. prepared samples and fabricated the devices. Y.W. assisted with the growth of VO_2. J.J. performed Raman mappings, photocurrent mappings and light polarization dependence measurements. Z.C. and Y.H. assisted photocurrent measurements and calibrations. Y.X. and L.Z. performed atomic force microscopy measurements. J.J. processed the data. J.J. and J.S. analysed and interpreted the results. J.J. wrote the paper. All the authors were involved in the discussion for data analysis. G.-C.W. and J.S. revised the manuscript. J.S. supervised the project.

Competing interests

The authors declare no competing interests.

Additional information

Supplementary information The online version contains supplementary material available at https://doi.org/10.1038/s41565-021-00919-y.

Correspondence and requests for materials should be addressed to J.J. or J.S.

Peer review information *Nature Nanotechnology* thanks the anonymous reviewers for their contribution to the peer review of this work.

Reprints and permissions information is available at www.nature.com/reprints.

Terms and Conditions

Springer Nature journal content, brought to you courtesy of Springer Nature Customer Service Center GmbH (“Springer Nature”).
Springer Nature supports a reasonable amount of sharing of research papers by authors, subscribers and authorised users (“Users”), for small-scale personal, non-commercial use provided that all copyright, trade and service marks and other proprietary notices are maintained. By accessing, sharing, receiving or otherwise using the Springer Nature journal content you agree to these terms of use (“Terms”). For these purposes, Springer Nature considers academic use (by researchers and students) to be non-commercial.
These Terms are supplementary and will apply in addition to any applicable website terms and conditions, a relevant site licence or a personal subscription. These Terms will prevail over any conflict or ambiguity with regards to the relevant terms, a site licence or a personal subscription (to the extent of the conflict or ambiguity only). For Creative Commons-licensed articles, the terms of the Creative Commons license used will apply.
We collect and use personal data to provide access to the Springer Nature journal content. We may also use these personal data internally within ResearchGate and Springer Nature and as agreed share it, in an anonymised way, for purposes of tracking, analysis and reporting. We will not otherwise disclose your personal data outside the ResearchGate or the Springer Nature group of companies unless we have your permission as detailed in the Privacy Policy.
While Users may use the Springer Nature journal content for small scale, personal non-commercial use, it is important to note that Users may not:

1. use such content for the purpose of providing other users with access on a regular or large scale basis or as a means to circumvent access control;
2. use such content where to do so would be considered a criminal or statutory offence in any jurisdiction, or gives rise to civil liability, or is otherwise unlawful;
3. falsely or misleadingly imply or suggest endorsement, approval , sponsorship, or association unless explicitly agreed to by Springer Nature in writing;
4. use bots or other automated methods to access the content or redirect messages
5. override any security feature or exclusionary protocol; or
6. share the content in order to create substitute for Springer Nature products or services or a systematic database of Springer Nature journal content.

In line with the restriction against commercial use, Springer Nature does not permit the creation of a product or service that creates revenue, royalties, rent or income from our content or its inclusion as part of a paid for service or for other commercial gain. Springer Nature journal content cannot be used for inter-library loans and librarians may not upload Springer Nature journal content on a large scale into their, or any other, institutional repository.
These terms of use are reviewed regularly and may be amended at any time. Springer Nature is not obligated to publish any information or content on this website and may remove it or features or functionality at our sole discretion, at any time with or without notice. Springer Nature may revoke this licence to you at any time and remove access to any copies of the Springer Nature journal content which have been saved.
To the fullest extent permitted by law, Springer Nature makes no warranties, representations or guarantees to Users, either express or implied with respect to the Springer nature journal content and all parties disclaim and waive any implied warranties or warranties imposed by law, including merchantability or fitness for any particular purpose.
Please note that these rights do not automatically extend to content, data or other material published by Springer Nature that may be licensed from third parties.
If you would like to use or distribute our Springer Nature journal content to a wider audience or on a regular basis or in any other manner not expressly permitted by these Terms, please contact Springer Nature at

onlineservice@springernature.com